Molecular Dynamics Simulations of the Human Ocular Lens with Age and Cataract

Joshua Fernandes,[1] Yalun Yu[2], and Jeffery B. Klauda[1,2*]

[1]Department of Chemical and Biomolecular Engineering, [2]Biophysics Graduate Program
University of Maryland,
College Park, MD 20742, USA

*Corresponding Author: jbklauda@umd.edu

Abstract

The human ocular lens consists primarily of elongated, static fibers characterized by high stability and low turnover, which differ dramatically in their composition and properties from other biological membranes. Cholesterol (Chol) and sphingolipids (SL) are present at high concentrations, including saturated SLs, such as dihyrosphingomyelin (DHSM). Past molecular dynamics simulations demonstrated that the presence of DHSM and high Chol concentration contributes to higher order in lipid membranes. This current study simulated more complex models of human lens membranes. Models were developed representing physiological compositions in cataractous lenses aged 74±6 years and in healthy lenses aged 22±4, 41±6, and 69±3 years. With older age, Chol and ceramide concentrations increase and glycerophospholipid concentration decreases. With cataract, ceramide concentration increases and Chol and glycerophospholipid concentrations decrease. Surface area per lipid, deuterium order parameters (S_{CD}), sterol tilt angle, electron density profiles, bilayer thickness, chain interdigitation, two-dimensional radial distribution functions (2D-RDF), lipid clustering, and hydrogen bonding were calculated for all simulations. All systems exhibited low surface area per lipid and high bilayer thickness, indicative of strong vertical packing. S_{CD} parameters suggest similarly, with saturated tails in the hydrophobic core of the membrane having elevated order. Vertical packing and acyl tail order increased with both age and cataract condition. Lateral diffusion decreased with age and cataracts, with the older and cataractous models demonstrating increased long-range structure by the 2D-RDF analysis. In future work examining the membrane proteins of the lens, these models can serve as a physiologically accurate representation of the lens lipidome.

1. Introduction

The human ocular lens is comprised of thin, relatively static fibers, and as such, its properties are controlled by the properties of the lipid membranes of these fibers.[1] The lipid composition of these fibers differs dramatically from other lipid membranes in humans, in part due to the need for stability over human lifespan of the lens.[2] These membranes also have higher than typical protein concentrations, which affect their properties.[3] The membranes of the ocular lens have a high concentration of cholesterol (Chol) and sphingolipids (SLs).[4] Specifically, there is an abundance of dihydrosphingomyelins (DHSMs), which are sphingomyelins (SMs) with a saturated sphingosine backbone.[5] DHSMs are known to be extremely stable lipids and among mammalian lenses, are only found widely in human lenses.[6] These lipids have been found to increase order within membranes and exhibit slow degradation. The effect of Chol on the lipid membrane in its liquid-disordered or -ordered phase is also an increase of order and the reported separation of the lipid membrane into cholesterol-rich domains (rafts).[7, 8] There is some evidence to suggest the presence of Chol domains within the ocular lens.[9]

Glycerolphospholipids (GLs) are also present in the human ocular lens, with head groups primarily consisting of phosphatidylethanolamine (PE), phosphatidylserine (PS), and phosphatidylcholine (PC).[10] These lipids also differ from typical membrane lipids, however, in that they are primarily not simple two-tailed acyl lipids. There are two principal forms GLs take in the human ocular lens, two-tailed plasmanyls and one-tailed ether lysolipids.[11] Plasmanyls have an ether *sn*-1 tail and a fatty acid *sn*-2 tail. Ether lysolipids, hence forth referred to as lysolipids, have an ether *sn*-1 tail and an alcohol moiety in the *sn*-2 position. It is believed that lysolipids may be the result of selective hydrolysis of the acyl chains of the plasmanyl lipids.[12]

Simplified molecular dynamics (MD) simulations of the human ocular lens have been performed using Chol, SMs, DHSMs, and GLs, including PCs and PEs.[13] These have shown the higher order provided by DHSMs as opposed to SMs and the effect on stability by increasing Chol in the lipid membrane. However, these simplified models fail to account for the variance of the lens lipidome with respect to changing age and formation of cataracts.

Profound changes occur within the lipid lens as humans age. The fetal ocular lens is primarily composed of GLs, and with age these GLs diminish while SLs increase.[14] In older individuals, lysolipids are the only GLs present in appreciable concentrations.[14] SMs and DHSMs remain relatively constant with age, with ceramides (CERs) and dihydroceramides

(DHCERs) increasing. Prior to age 20, these lipids are negligibly present within the human ocular lens but become the most widely prevalent non-Chol lipids by age 60.[14] CERs are dephosphorylated SMs, and as such have small head groups, contributing to spontaneous negative curvature of membranes and may reduce headgroup packing of a membrane.[15] The mechanism of their formation within the human ocular lens is not entirely known, although it is possible that they may be present due to oxidation of the SMs and DHSMs within the lens, as they show similar distributions of tail lengths as SMs and DHSMs.[14] Chol increases with age in healthy lens tissue until eventually Chol crystals form within the ocular lens due to saturation of the lipid membranes.[16]

Cataracts are a significant disease of the ocular lens where regions of the lens become opaque, leading to cloudy vision or blindness. Only small structural changes within the lens such as a very low concentration of multilamellar bodies (MLBs) are needed to cause serious cataracts.[17] In nuclear cataracts, there may be no physical barrier to light, and instead, biochemical changes within the lens may lead to opacity due to scattering.[18] These may include irregular lipid structure, such as undulating membranes, which are likely caused by aggregation of crystalline proteins.[19] The proteins distribute asymmetrically across the membrane leading to propensity to nonzero curvature.[20] Cataracts are associated with significant changes in ocular lens composition, with an increase of CER concentration,[21] as well as a sharp decrease in GL concentration.[22] In addition, Chol concentration within the membrane decreases, although it is also suggested that Chol crystals are present in cases of cataracts, indicating that Chol solubility in cataractous lens membranes may decrease.[23]

By using this information to develop models that more accurately depict the evolving lipidome of the human ocular lens, MD simulations can be used to understand the effect of lipid composition changes on membrane structure. In this work, four models of ocular lens composition in humans at different ages, with and without cataracts, were developed from literature. These models were then constructed for all-atom simulations using NAMD. This work seeks to extend previous simulations of lens membranes and identify changes observed with age and cataract in the properties of lens membranes, including membrane thickness, order parameters, interdigitation, and radial distribution functions.

2. Methods

2.1. Model compositions

Models were developed for healthy and cataractous lenses based on the phospholipid headgroup distributions found by Huang and Estrada.[11, 22] From this data, healthy lenses were modeled at three ages: 22±4, 41±6, and 69±3 years. Cataractous lenses were modeled for ages 74±6. Tail lengths and saturations were determined from the results of Deeley, simplifying to only consider lipids with over 5% concentration in the lens.[24] From the results of Mainali, Chol/PL ratios were used to determine the Chol concentration,[16, 23, 25] and the results of Hughes were used to find the concentrations of CER and DHCER for healthy lenses.[14] For cataractous lenses, the results of Tao and Cotlier were used to find CER and DHCER concentrations.[21] Together, these results give the models shown in Table 1. The structures of the 10 lipids selected for the models are shown in Figure 1. These models balance head group concentration, tail length, and relative abundance for lipids with composition at least 5%. Membrane hydration was selected to give at least 30 water per cholesterol and 40 per all other lipids. All systems had leaflets with symmetric compositions.

Table 1. Membrane model lipid amounts per leaflet with the lipid fraction shown in parenthesis.

System	**Young Adult (Y)**	**Middle-Aged (M)**	**Older-Aged (O)**	**Cataractous (C)**
Lipid	Healthy *Age*=22±4	Healthy 41±6	Healthy 69±3	Cataractous 74±6
Chol	45 (0.474)	64 (0.552)	65 (0.565)	32 (0.390)
DOPEP	9 (0.095)	6 (0.052)	6 (0.052)	-
OPEL	11 (0.116)	8 (0.069)	7 (0.061)	5 (0.061)
SOPS	5 (0.053)	-	-	-
PSM	5 (0.053)	6 (0.052)	5 (0.043)	5 (0.061)
DHPSM	12 (0.126)	15 (0.129)	10 (0.087)	9 (0.11)
DHNSM	8 (0.084)	12 (0.103)	6 (0.052)	6 (0.073)
CER160	-	-	5 (0.043)	7 (0.085)
DHC160	-	5 (0.043)	6 (0.052)	11 (0.134)
DHC241	-	-	5 (0.043)	7 (0.085)
Water (total)	6650	7752	7820	5904

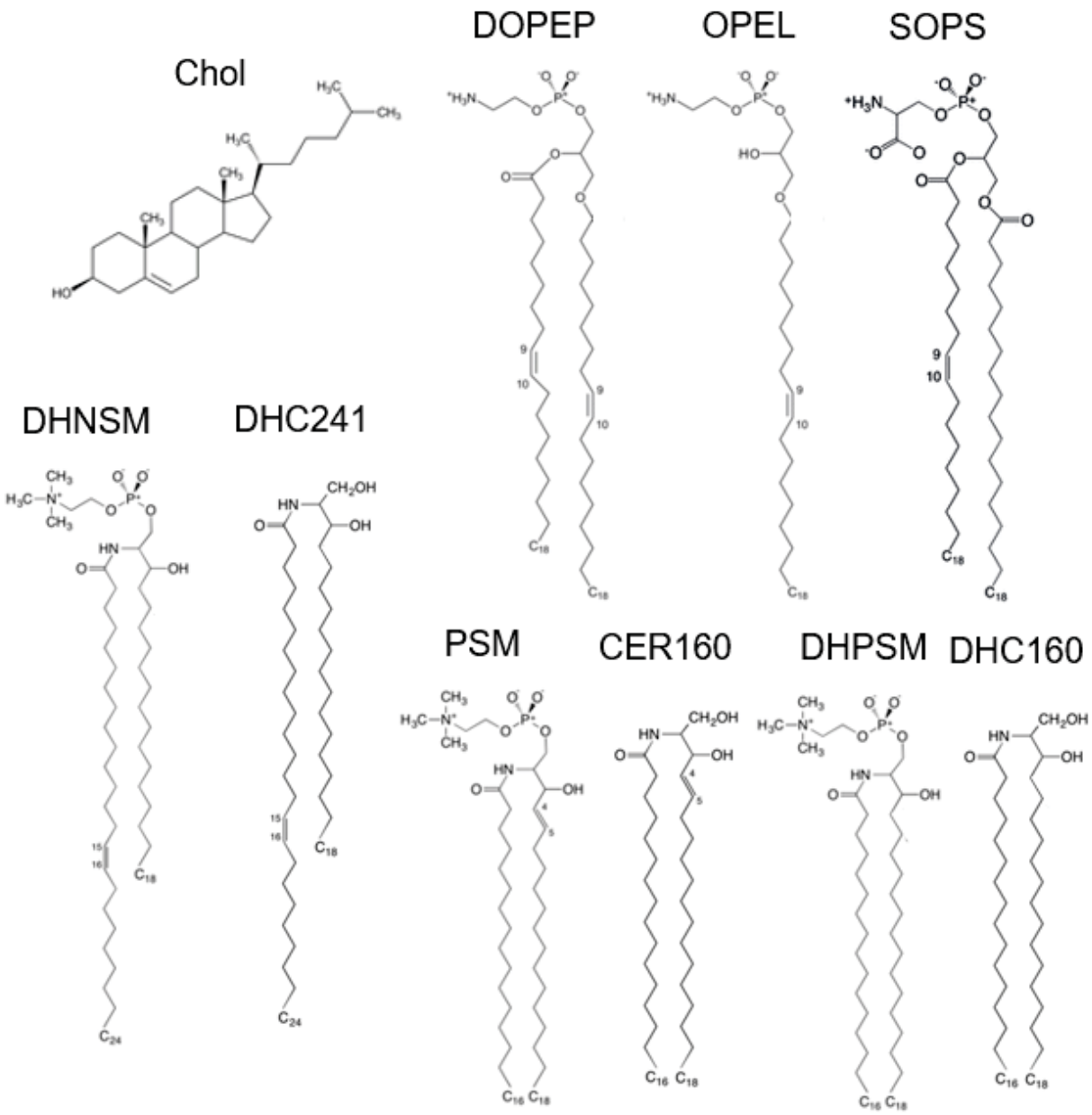

Figure 1. The 10 lipids present in the 4 models simulated within this work.

2.2. System setup and simulations

Systems were simulated at a temperature of 37ºC and a pressure of 1 atm for a time of 750 ns. Neutralizing K^+ ions were used in the young system to maintain charge neutrality with the negatively charged PS head groups. A hydration number between 34 and 36 was used relative to all lipids for each system to ensure adequate hydration. Simulations verified the total water region to be greater in thickness than the bilayer, suggesting that this was sufficient. The CHARMM-GUI

Membrane Builder was used to generate three replicas per model and equilibration was performed using a six-step process in NAMD.[26-29] Each replica was randomly generated with a distinct initial configuration. Figure 2 shows visualizations of one replica of each of the four models, at the end of the simulated trajectory. Force field parameters for dihydrosphingolipids (DHSMs and DHCERs) were produced from the existing parameters in the CHARMM36 force field for their standard SL counterparts (SMs and CERs).[30, 31] The parameters and topology for the plasmanyl lipid, DOPEP, was made by combining the existing force fields for the standard acyl lipid, DOPE, and ether lipid, DOPEE.[32] The topology and parameters for the lysolipid, OPEL, was made by replacing the *sn*-2 tail of the force field for DOPEE with the alcohol group from the glycerol model. Snapshots were produced using Visual Molecular Dynamics (VMD).[33]

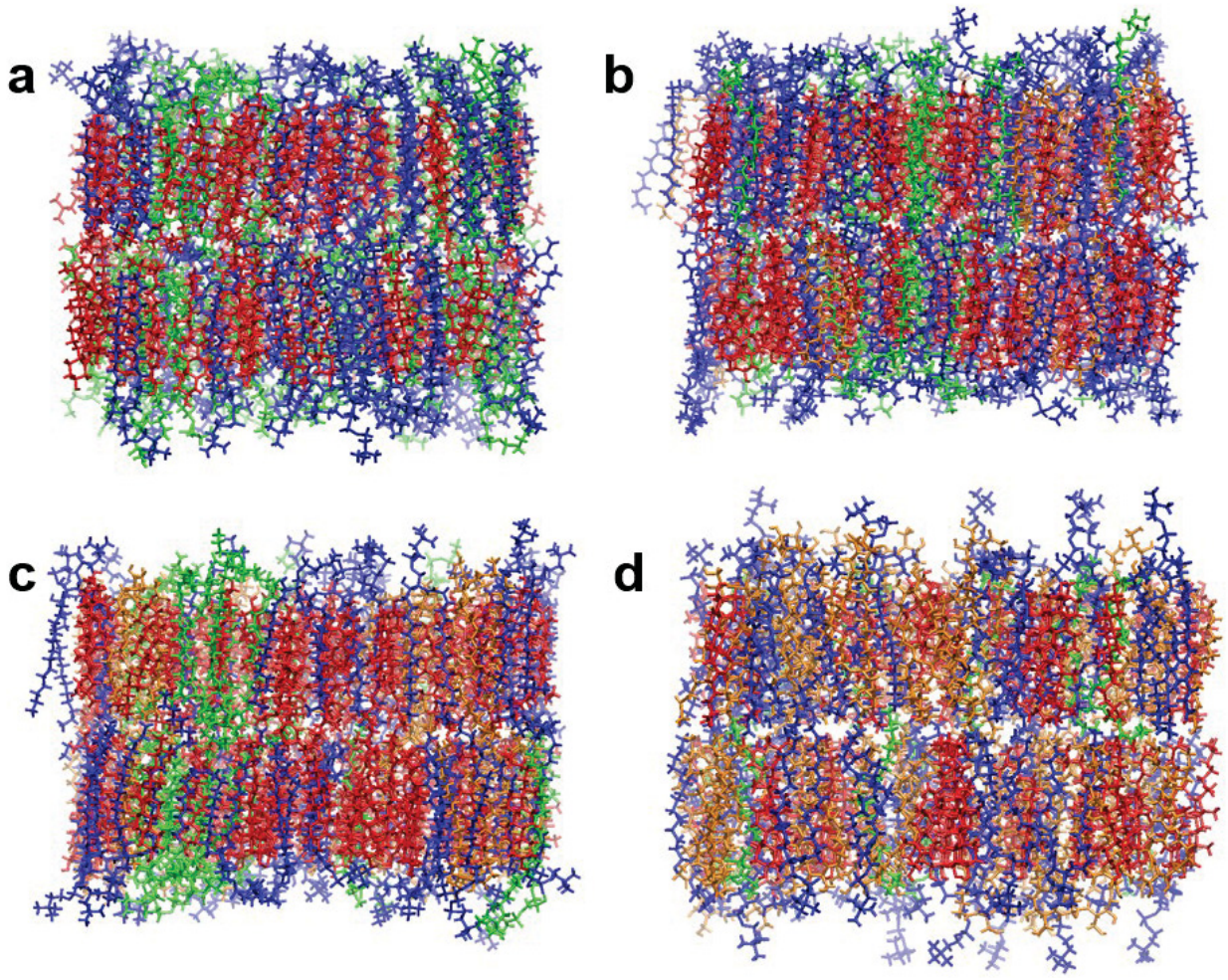

Figure 2. Snapshots from the first replicates of each of the four models. Red indicates Chol, blue SM, green GL, orange CER. (a) Young adult model, (b) middle-aged model, (c) old-aged model, (d) cataractous model. Waters are omitted for clarity.

2.3. Analysis

Analysis was performed on the final 250 ns of each model with results averaged across replicates. Analyses performed include surface area per lipid (SA/lip), compressibility, component area per lipid, deuterium order parameters (S_{CD}), sterol tilt angle, electron density profiles (EDPs), bilayer thickness, interdigitation, two-dimensional radial distribution functions (2D RDFs), mean-square displacement (MSD), lipid clustering, and hydrogen bonding (H bonding). These were run using CHARMM, Python, VMD, and C. All errors were computed by standard error from the mean of the three replicates for each system.

SA/lip was calculated by calculating box area and dividing by number of lipids per leaflet. The area compressibility modulus (K_A) was calculated by taking the time-averaged variance in SA/lip using the expression

$$K_A = \frac{k_B T \langle A \rangle}{N \sigma^2_{\langle A \rangle}} \quad (1)$$

where k_B is Boltzmann's constant, T is temperature, $\langle A \rangle$ is the average surface area of the membrane, N is the number of lipids per leaflet, and $\sigma^2_{\langle A \rangle}$ is the variance in total surface area.

Component surface area per lipid was calculated by constructing 2D Voronoi cells in the plane of the membrane for the C2, C21, C31 atoms for GLs, the C2S, C1F, and C4S atoms for SLs, and the O3 atom for Chol.[34] Summing the polygon areas for each lipid and averaging gave the surface area per each component in the system. S_{CD} was calculated by the formula

$$S_{CD} = \left| \langle \frac{3}{2} \cos^2 \theta - \frac{1}{2} \rangle \right| \quad (2)$$

where θ is the angle between the C-H bond and the bilayer normal. For carbons with multiple hydrogens, the average of all C-H bond directions was calculated. Sterol tilt angle was calculated by determining the angle between the vector defined by C3 and C17 of cholesterol and the bilayer normal. For the lysolipid OPEL, which lacks the C21 atom, only the C2 and C31 atoms were used.

EDPs were calculated by first reorienting the box so that the center of the bilayer was set to Z=0. Using slabs of 0.2 Å in width, electron density was calculated for each height Z above and below the center. Densities were then grouped according to lipid and by functionalities. Three

thicknesses were calculated using the EDPs. Overall bilayer distance (D_B) was calculated as the distance between the two points where the water density was half its maximum. Headgroup-to-headgroup distance (D_{HH}) was calculated as the distance between the two peaks in total density, corresponding to the electron-dense phosphate headgroup region. Hydrophobic distance ($2D_C$) was calculated as the distance between the two points where the density of the hydrocarbon tails was at half its maximum. Interdigitation for each lipid was also calculated from density profiles, according to the following length parameter defined by Das et al.[35]

$$\lambda_{ov} = \int_{-L}^{+L} 4 \frac{\rho_t(z)\rho_b(z)}{(\rho_t(z)+\rho_b(z))^2} dz \quad (3)$$

where λ_{ov} is the interdigitation parameter, ρ_t is the density of the lipid in the top leaflet, ρ_b is the density of the lipid in the bottom leaflet, and L is the length of the overlap region (50 Å was used here).

2D-RDFs for self-interactions were calculated using the phosphate group of phospholipids, the alcohol headgroup of ceramides and the alcohol headgroup of cholesterol. The radial step used was 0.1 Å. For pairwise RDFs between phospholipids and ceramides, the same headgroups were used. For pairwise interactions involving cholesterol, the alcohol headgroup of cholesterol and the second methyl group of the lipid tail of the non-cholesterol lipid were used. This was chosen because it was the methyl group closest to the average horizontal plane occupied by the cholesterol's alcohol moiety. Mean-square displacement was calculated using average head group position, with a reset frequency of 5 ns to smooth the data. Due to lateral movement of each leaflet, position was measured relative to the center of mass of each leaflet. Displacement was then calculated as the change in this relative position of an individual lipid.

Lipid clustering was calculated using the DBSCAN algorithm[36] with headgroup-specific cutoff distances of 6.24 Å for PLs, 4.6 Å for CER, and 5.75 Å for Chol, as determined from the first peak of the radial distribution functions. For dissimilar lipids, an averaging of the headgroup size was utilized. Clusters were defined as three or more lipids meeting these cutoff distances within a given frame. Both intra- and intermolecular hydrogen (H) bonds were considered. H bonds were any pair with a donor-acceptor distance of less than 2.4 Å with a donor-acceptor angle greater than 150°.

3. Results

3.1. Surface Area per Lipid (SA/lip) and Compressibility

SA/lip was used as a metric for equilibration. Beginning with SA/lip between 42 and 44 $Å^2$, all systems equilibrated to SA/lip between 39 and 40 $Å^2$ within approximately 250 ns (Figure S1). SA/lip was relatively stable after this point, with the cataractous replicates showing the slowest equilibration. Two of these replicates continued to show diminishing SA/lip beyond 300 ns in the 750 ns simulations (Figure S1j-k). However, there was no indication of a trend within the final 250 ns (used for analysis) within these replicates. In the young adult system, an apparent decreasing trend was seen in the final 250 ns, so an additional 250 ns of simulation was performed which ended the apparent trend (Figure S1a). The final 250 ns of the 1000 ns simulation was used for analysis of this replicate.

The middle-aged and older-aged models showed a decrease in SA/lip from the young adult model, as expected due to increased Chol concentration (Table 2). The middle-aged and older-aged models were expected to show similar areas due to similar Chol compositions, which matches observed results. With cataract, SA/lip was slightly higher than in the middle-aged and older-aged systems. However, this model was characterized by a significant decrease in Chol concentration from the healthy systems and would be expected to significantly increase in SA/lip. Thus, the minimal change in SA/lip, coupled with the slower equilibration of the cataractous replicates, suggest that the cataractous membranes have a greater degree of order and rigidity. The additional concentration of CER lipids is likely the cause of the decrease in SA/lip due to the ability of CER lipids to pack well. Across replicates, there was very strong consistency.

The area compressibility modulus showed very rigid membrane systems. Pure PL systems typically have moduli less than 1 N/m.[37] Systems with Chol often have higher area compressibility moduli due to better packing in the hydrophobic core.[38] A similar result is seen in systems with high CER concentrations. This is consistent with the results observed here, as all four models show high compressibility moduli. The young adult system has a modulus significantly lower than the other three, but this is still in a more ordered rigid state than the liquid-disorodered state that typically see compressibility moduli around 0.3 N/m [37] (Table 2). The middle-aged, older-aged, and cataractous systems all showed similar area compressibility moduli

and these measurements had a wide degree of variation between replicates. The values are consistent with similar systems containing GLs, SMs, Chol, and CER.[39]

Table 2. Overall SA/lip and area compressibility modulus for all systems. Y=young, M=middle aged, O=old and C=cataractous,

	Y	**M**	**O**	**C**
SA/lip ($Å^2$)	39.72±0.05	38.95±0.06	39.14±0.02	39.3±0.1
$\mathbf{K_A}$ (N/m)	1.3±0.1	2.5±0.4	2.3±0.2	2.5±0.2

3.2. Component Surface Area per Lipid

Surface area per lipid was seen to be consistent for each lipid between the healthy models. For each lipid, the cataractous models showed a decrease in component surface area, consistent with the results for overall SA/lip (Table 3). DOPEP showed the highest surface area per lipid, followed by SOPS. All SMs and CERs showed similar areas per lipid regardless of head type and tail length. The one-tailed ether lipid maintained a significantly lower surface area of 39 $Å^2$. Chol maintained a surface area between 25-30 $Å^2$, on the lower end of the expected Chol surface area per lipid.[13] This indicates a greater degree of vertical structure in the lipid membranes as compared to typical Chol-containing membranes.

Notably, the youngest models had a lower Chol surface area per lipid than the other healthy models. A possible explanation is the decreased Chol concentration in the youngest models, allowing for stronger interactions of Chol with other molecules, diminishing the area occupied by Chol. Applying this reasoning to the cataractous system can also explain the further diminished surface area of Chol in those models, where Chol concentration is lowest. This is consistent with the observation of Chol reaching saturation in cataractous lenses, as it is possible that further Chol concentration within the cataractous models would not stabilize the system but rather result in separate domains.

Table 3. SA/lip for each component in all systems in $Å^2$.

	Y	**M**	**O**	**C**
Chol	28.0±0.2	29.8±0.1	30.0±0.1	26.4±0.5
DOPEP	58.4±0.1	58.7±0.5	58.8±0.6	-
OPEL	39.2±0.3	39.4±0.2	38.7±0.2	36.5±0.5
SOPS	55.2±0.2	-	-	-
PSM	50.5±0.4	51.9±0.5	51.5±0.4	47.9±0.5
DHPSM	51.4±0.4	52.0±0.1	52.5±0.4	49.4±0.6
DHNSM	52.5±0.6	52.0±0.5	51.3±0.8	49.1±0.5

CER160	-	-	51.5±0.8	47.5±1.2
DHC160	-	51.1±0.5	52.6±0.8	48.8±0.4
DHC241	-	-	52.5±0.4	49.1±0.2

3.3. Deuterium Order Parameters (S_{CD})

The deuterium order parameters of saturated lipid tails show a very high degree of order. In the hydrophobic core of the membrane, order parameters exceed 0.4, with the highest values achieved by the cataractous models (Figure 3). Across most lipids, order parameters increase with increasing age. As expected, the DHSMs and DHCERs show high order in the saturated C4 and C5 positions of the sphingosine backbone (Figure 3c-d), whereas SMs and CERs are characterized by a steep drop in this location where the unsaturation is present (Figure 3b). In carbons close to the headgroup on the sphingosine tail, higher order is observed in the unsaturated lipids, while the saturated lipids show a sharp decrease in order parameter near the headgroup. This may correspond to the double bond separating behavior of the carbons above and below the double bond, stabilizing headgroup interactions, while the free movement of the DHSMs and DHCERs allows for greater flexibility and a lack of stability among the carbons adjacent to the headgroup. In addition, the carbons adjacent to the headgroup are most stable in the models with lowest age, suggesting that the increased GL composition allows for greater headgroup stabilization by intermolecular interactions (likely hydrogen bonds).

All lipid tails are 18 carbons or shorter with the exception of the fatty acid tails of DHNSM and DHC241 (Figure 1). Both have a nervonic acid (24:1 Δ15) tail. The unsaturation results in a strong drop in order parameter at the position of unsaturation (Figure 3c). Beyond the unsaturation, there is no strong increase in order parameter toward the center of the membrane. By the terminal methyl group, it increases slightly, but after this point, the order parameter approaches 0. This would suggest free rotation with no preferential orientation. Since the 24-carbon tail is longer than other tails present, it can lend itself to several possible configurations. One possibility is a hooked conformation, where the lipid tail bends at the centerline, folding on itself at the middle of the membrane, while another is a straight configuration, where the lipid interdigitates with the other leaflet. The decrease in order parameter suggests that the former likely is the better descriptor of the lipid orientation, since there is no evidence of order (see Section 3.6). Strong interdigitation would result in a high degree of order among the later carbons on the nervonic acid tails.

Unsaturated SLs show the expected dip in order parameter at the points of unsaturation, C4 and C5, while the saturated SLs (DHSM and DHCER) show an increase in order parameter to near that of the hydrophobic core. This suggests that the region is not limited by interactions with the unsaturated SLs and high order can be achieved despite potential neighboring with less ordered lipids.

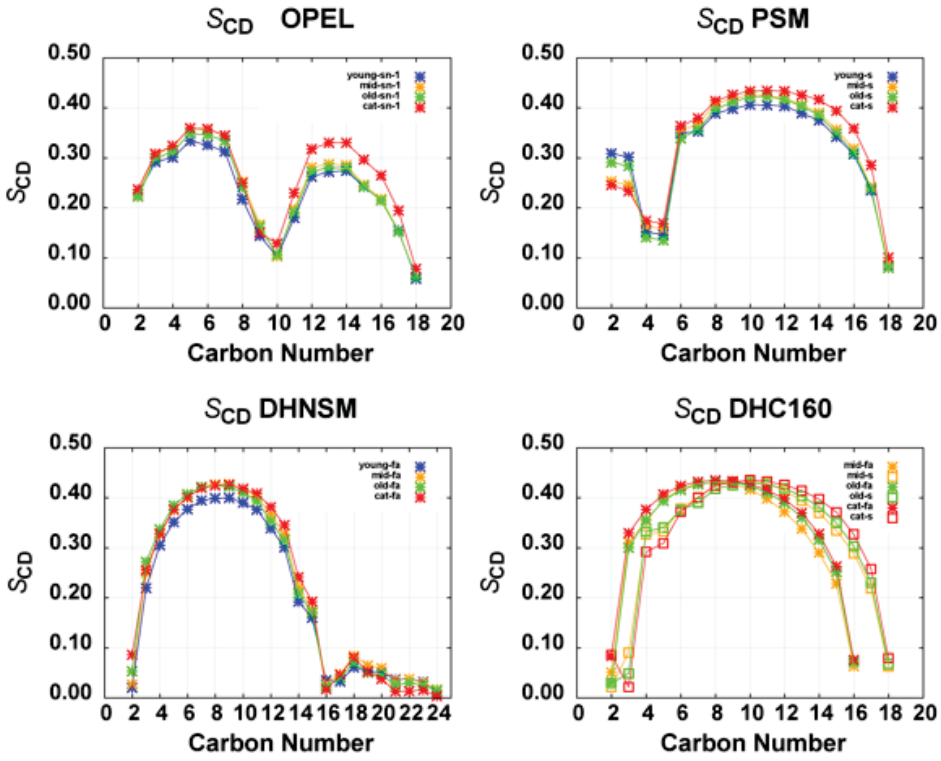

Figure 3. Selected plots of order parameter for particular lipids, including (a) the one tail of OPEL (*sn*-1), (b) the sphingosine tail of PSM, (c) the 24-carbon fatty acid tail of DHNSM, and (d) both tails of DHC160.

3.4. Sterol Tilt Angle

The sterol tilt angle gives a measure of vertical stability of the lipids in the membrane, as with the deuterium order parameters. The median sterol tilt angle of 9.0° for the cataractous system indicates sterols in very vertical orientation, with the median tilt angle of 10.7° in the young healthy system indicating a lower, but still high level of verticality (Figure 4). In addition to having a higher average tilt angle, the young-aged model also has a more skewed right distribution of tilt angles.

Of note is that the very similar tilt angle distributions of the middle-aged and older-aged healthy models may suggest similar levels of sterol vertical organization in the membrane. Given the similar lipid distribution, this is perhaps unsurprising, as Chol is known to pack more deeply in the hydrophobic region of the membrane. The major change between the middle-aged and older systems is a replacement of SM lipids with CER lipids, which affects only headgroups. Thus, unless a significant change in stability occurred from changing headgroup interactions, it would be expected that the Chol packing and distribution would be similar between the two models.

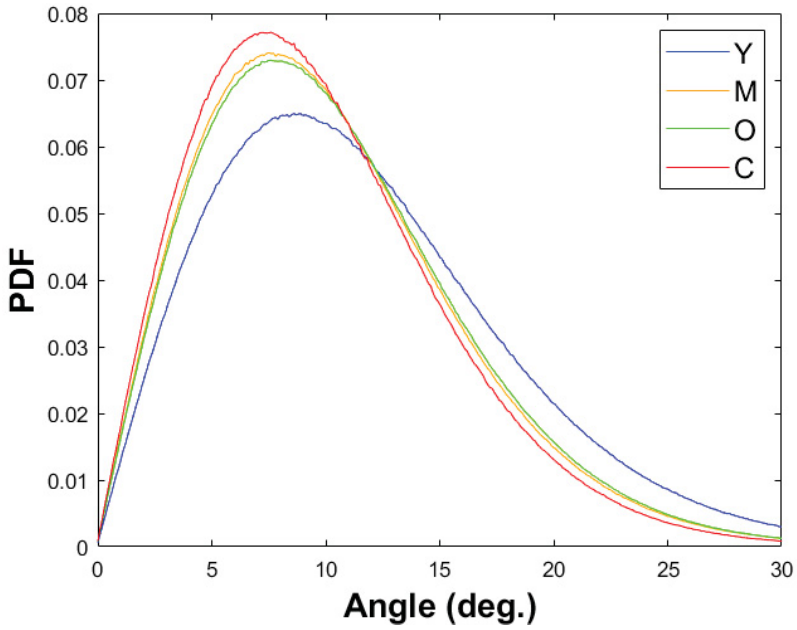

Figure 4. The distributions of Chol tilt angles for all four models.

3.5. Electron Density Profiles (EDPs), Bilayer Thickness

The averaged electron density shows a maximum peak near 24 Å in all models (Figure 5). This corresponds to the location of the phosphate group within the GP and SM lipids. Another peak appears around 20 Å corresponding to the CER headgroups and glycerol backbones. As expected, for older-age models and cataractous models with lesser phospholipid and greater CER concentration, the peak at 20 Å increases in relative size. In the youngest models, it appears merely as an inflection point (Figure 6a). Around 10 Å another peak appears, corresponding to the maximum of the hydrophobic core (Figure 6). This peak manifests due to the high Chol concentration, which packs tightly within the membrane, leading to a dip between the maximum from the headgroups and the maximum from the hydrophobic core. The 10 Å peak is greatest for

the middle- and older-aged healthy systems, which have the greatest concentration of Chol. It is smallest in the cataractous systems, which have the lowest Chol concentration.

At the centerline, there is a strong decrease in electron density to about 60% of the baseline water value and 50% of the maximum value. Such a drop is characteristic of highly ordered membranes. Whereas a more randomly ordered membrane will have many chains crossing the bilayer centerline, a more tightly packed membrane will begin to form a gap between the leaflets as it enters a liquid-ordered or liquid-crystalline phase. For these systems, the density does not get very near zero because of the presence of the 24-carbon tailed SM and tail interdigitation (see Section 3.6).

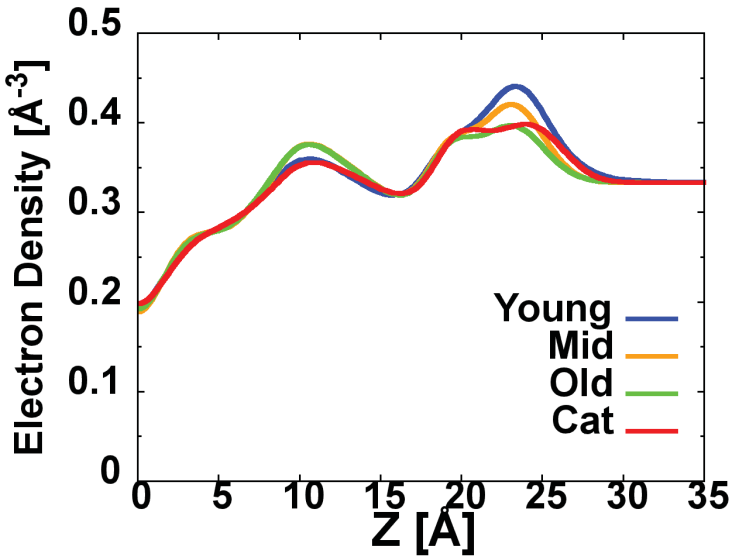

Figure 5. A comparison of the total EDPs of the four systems surveyed.

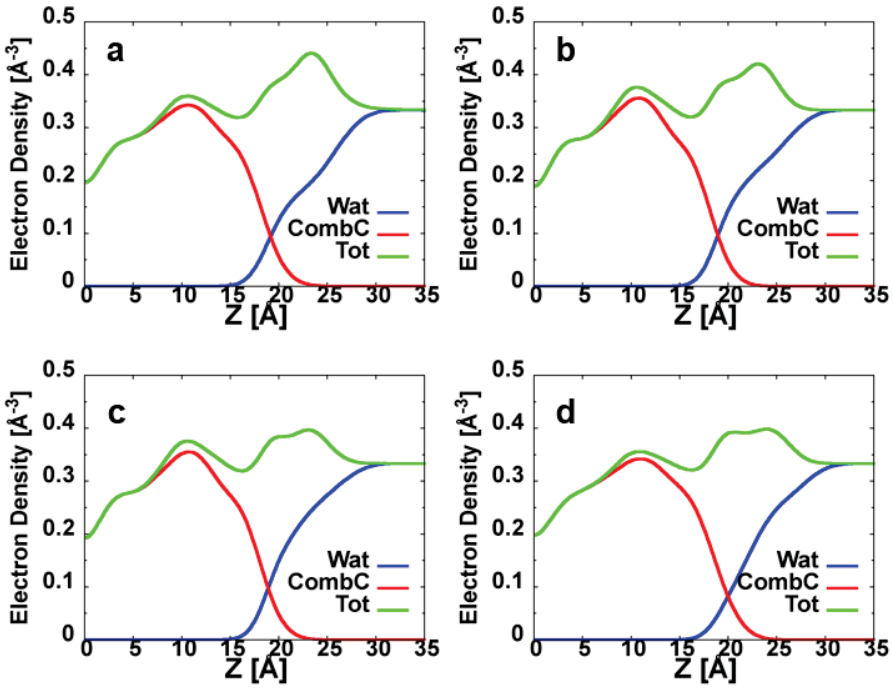

Figure 6. EDPs for the (a) young adult, (b) middle-aged, (c) older-aged, and (d) cataractous models with water density and hydrocarbon density shown.

The thickness was observed to be highest in the cataractous system, followed by the young-aged healthy system, with similar values in the middle- and older-aged systems (Table 4). The cataractous system showing the greatest thicknesses is consistent with the high degree of vertical order in the cataractous models. Very rigid lipids lead to tight packing and elongated lipids, creating greater thickness. The young-aged system, which demonstrated a lower degree of vertical order nonetheless demonstrated higher thicknesses solely due to possessing, on average, larger lipids. The higher concentration of GLs with PE headgroups led to a higher thickness despite a lower degree of vertical order, especially when coupled with the absence of small CER lipids that were present in the middle- and older-aged systems. All three calculated thicknesses demonstrated similar behavior.

Table 4. Membrane thicknesses for all systems in Å. D_{HH} is headgroup-to-headgroup distance, D_B is overall bilayer distance, and $2D_C$ is the hydrophobic core thickness.

	Y	M	O	C
D_{HH}	46.73±0.18	46.20±0.12	46.27±0.07	47.87±0.07
D_B	43.29±0.10	41.39±0.05	40.98±0.03	44.66±0.13
$2D_C$	35.54±0.03	35.11±0.03	35.11±0.03	36.55±0.05

3.6. Interdigitation and Terminal Methyl Distribution

The 24-carbon acyl tail of the DHNSM lipid was expected to interdigitate with the other leaflet. Of interest was whether it remained straight and entered into hydrophobic interactions with the acyl tails of the opposing leaflet or if it kinked to have a random coil movement in the interleaflet space. Figure 7 shows highlighted DHNSM lipids, some of which maintain verticality and interdigitate, while the majority hook in the interleaflet space. Evidence suggests that the hook, or kinked, conformation was more prevalent. This would lead to a comparatively disordered membrane center, allowing for better movement and transport within this layer compared to the well-packed bulk. In addition, the prevalence of the hooked conformation tails is consistent with the observation of a decrease in electron density at the bilayer center. This also suggests that the center of the bilayer will take a more fluid phase compared to the highly ordered hydrophobic core consisting of mostly saturated lipids and cholesterol, as seen in the deuterium order parameters for the 24-carbon acyl tails.

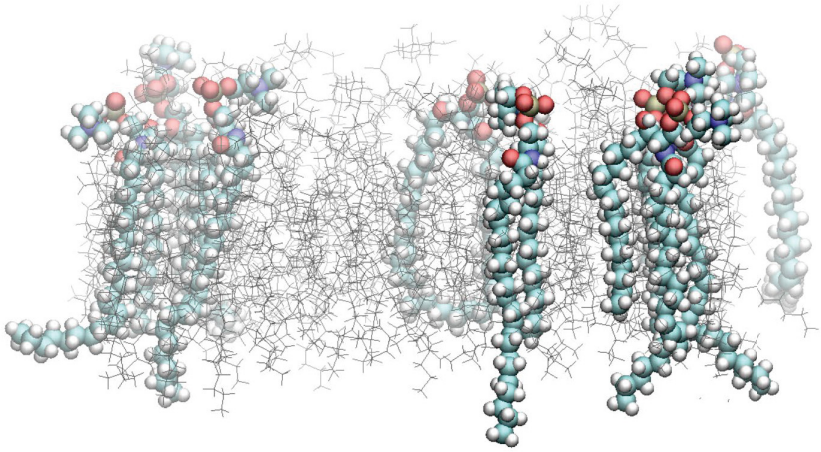

Figure 7. A snapshot of the upper leaflet of the first young adult model replicate with the DHNSM lipids highlighted. Some show the interdigitating behavior while others show the hook conformation at the interleaflet interface.

The interdigitation parameter given by Eq. (3) was calculated for all constituent components. In general, smaller lipids demonstrated less interdigitation (Table 5). The parameter gives an estimate on the average length of interdigitation, with the 24-carbon tailed lipids by far having the highest values for interdigitation across all systems. This was followed by the GL lipids, likely due to the 18-carbon tails compared to the 16-carbon tails of the other SM and CER lipids.

Chol also showed comparable interdigitation to the CER lipids, likely due to Chol's ability to penetrate deeper into the bilayer due to a lack of a strongly polar headgroup. For the same reason CER was able to interdigitate to a greater extent than SM among the 16-carbon tailed SLs.

Interdigitation was relatively consistent between the three healthy systems, but a significant drop in interdigitation was observed in the cataractous system. The high degree of verticality in the cataractous membranes may result in less tail space available to penetrate. In addition, the tight packing may cause more difficulty for the lipid tails to penetrate the other bilayer resulting in a greater degree of bunching of excess tails within the interleaflet region in the cataractous system.

Table 5. Interdigitation parameters for each of the components in each system.

	Y	**M**	**O**	**C**
Chol (Å)	2.67±0.05	2.41±0.03	2.54±0.03	2.36±0.03
DOPEP (Å)	3.56±0.05	3.82±0.06	3.74±0.07	-
OPEL (Å)	3.43±0.04	3.35±0.04	3.44±0.03	3.0±0.1
SOPS (Å)	4.04±0.05	-	-	-
PSM (Å)	1.96±0.02	1.88±0.05	1.96±0.02	1.66±0.03
DHPSM (Å)	2.14±0.02	1.98±0.03	2.03±0.03	1.9±0.01
DHNSM (Å)	7.63±0.07	7.76±0.09	7.8±0.1	6.6±0.2
CER160 (Å)	-	-	1.94±0.04	2.02±0.04
DHC160 (Å)	-	2.18±0.01	2.08±0.06	1.9±0.03
DHC241 (Å)	-	-	7.26±0.04	6.6±0.04

The average vertical location of the terminal methyl of the 24-carbon tails of the DHNSM and DHC241 were tracked over the trajectories where $Z<0$ corresponds to the terminal methyl group crossing the bilayer center (Figure 8). In all the models, the average position of the terminal methyl group of these lipids is across the bilayer center. This indicates that there is some level of interdigitation between the leaflets. However, due to the decreases observed in the electron density and the order parameters at the bilayer center, it is possible that the interleaflet space consists of a more fluid mixture of the 24-carbon tails, rather than true interdigitation between the leaflets. The middle-aged and older-aged models show the longest distance across the bilayer center, which is consistent with the calculated interdigitation parameters. In addition, there is not an obvious trend in the average position in the young, middle, and older aged models, with fluctuations up and down as individual lipids changed their conformations in the replicates. There is a decreasing trend in the cataractous model over the simulation trajectories which may be indicative of a slower

timescale of conformational changes in this model. It is possible that this increased timescale for interdigitation may be responsible for the lower measurement of the interdigitation parameter for the cataractous model. Over the last 250 ns of the cataractous models, the average position appears stable, which may suggest approach to an equilibrium distribution of tail conformations.

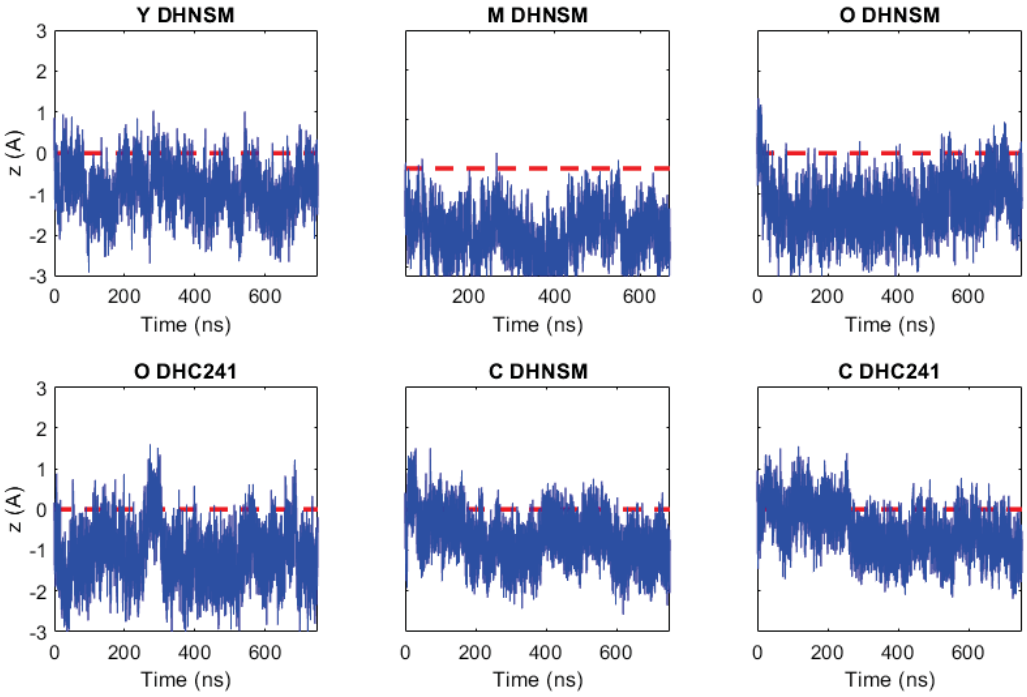

Figure 8. Average terminal methyl position for the 24-carbon tailed lipids, DHNSM and DHC241, for each of the four models. Z=0 is defined as the bilayer center with Z<0 corresponding to the tail penetrating to the opposing leaflet.

3.7. 2D Diffusion and Mean Square Displacement (MSD)

Lateral diffusion of the lipids in the bilayer was assessed via MSD calculations. It should be noted that the diffusion constants are not what is measured experimentally due to periodic boundaries and hydrodynamic effects,[40, 41] but our calculations can be used to compare between different ocular lens models. Diffusion calculations were relatively consistent between replicates and showed linear behavior for times beyond 5 ns. Diffusivities were calculated for each lipid, although past research has shown that diffusivities can be off by an order of magnitude or more in small simulations. Due to the periodic boundary conditions, self-interactions can occur, leading to inaccuracies in measurement of membrane properties. However, given the consistency between

replicates, it is reasonable to compare the results between the models presented here. The youngest-aged models demonstrated the greatest lateral lipid diffusion, with a Chol diffusivity of 6.91×10^{-9} cm^2/s (Figure 9). The middle-aged and older-aged healthy models showed similar diffusivities, with a slightly greater Chol diffusivity in the older-aged model. Finally, the cataractous model showed the lowest diffusivity, with roughly half of the older-aged models and a quarter of the youngest-aged models. This result is consistent with results suggesting higher order within the cataractous and older-aged models, as a greater degree of structure would result in less mobility within the bilayer.

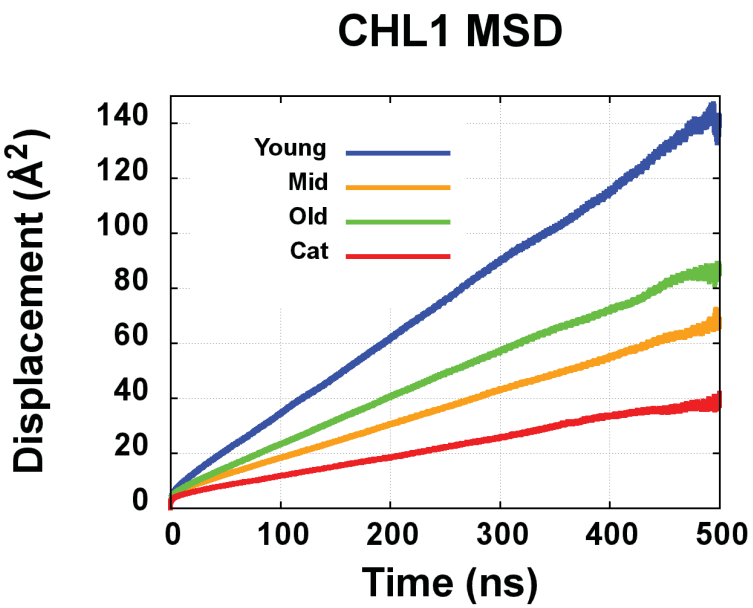

Figure 9. Mean-squared displacement plots in the 2D profile of the membrane for Chol in each of the systems.

On very short timescales, a pattern of anomalous diffusion was observed. This phenomenon is associated with a non-linear dependence between MSD and time. Within approximately the first 5 ns, diffusion on the order of between 0.22 and 0.32 was observed in all replicates (Figure S2). This is possibly indicative of a transition period from molecular ballistic motion to normal diffusion. A transition from anomalous subdiffusion to normal diffusion in protein-free membranes has been noted by other authors, although on longer timescales than observed here of up to hundreds of nanoseconds.[42] In addition, the authors found that high concentrations of Chol could lead to anomalous diffusion on the order of 100 ns, which is not seen here despite the presence of Chol in high concentrations.[43] Within these simulations, the short

timescale displacements are likely due to the rattling of lipids within a cage formed by their neighbors. Thus, they are representative of molecular motion rather than a diffusive process.

3.8. Lipid Clustering and 2D Radial Distribution Functions (2D RDFs)

2D RDFs for Chol-Chol self-interactions were used to assess equilibration of the lateral structure of the membrane systems. These were chosen, as Chol was the most abundant lipid. Convergence of the RDFs was determined by comparisons between blocks of 5 ns at the end of the trajectories and across replicates of a given model (Figure S3). All individual replicates showed convergence within 750 ns, with stabilization of the RDFs within the final 250 ns or earlier. Some small deviations were observed, but these diminished along the simulation trajectory. All healthy models also showed strong consistency across replicates, with similar convergence in number of peaks and peak heights (Figure S3a-i). However, weaker convergence was seen in the cataractous models, where peak height varied more significantly between the replicates (Figure S3j-l). Despite this discrepancy, number of peaks was roughly constant between the cataractous replicates, as was location of peaks. In addition, the cataractous system showed the weakest convergence of the RDFs within each replicate. This may be indicative of a slower timescale of equilibration for the cataractous system. However, despite larger deviations in the RDFs for the cataractous model, the final 250 ns of each of the three replicates shows greater stability and similarity to the other replicates than earlier RDFs from these trajectories. For example, the lightest gray curves of Figure S3j-l show greater differences than the red curves, corresponding to the last 250 ns of each replicate.

For the Chol RDFs, significant long-range structure was seen in all systems (Figure 10a). The youngest system showed three peaks, with potentially a fourth one. Similar results were seen for the middle-aged and older-aged systems as well, with the peak distance slightly larger for these systems. The cataractous system demonstrated the greatest long-range structure, with five well-defined peaks and a shorter distance between peaks. This suggest greater regularity in the organization of the cataractous system than the others, which may be consistent with previous results on greater structure and crystallinity within the cataractous system.

In the SM RDFs, only two peaks were well defined, with distances of 6.2 Å and 8.7 Å (Figure 10d). This result matches previous work which found two peaks, corresponding to two different interactions between SM headgroups at approximately the same distances. Quickly after

the second peak, the RDF went to 1 in all models, suggesting no longer-range structure, or overlap of conformations due to the distinct interaction conformations.

In the PE RDFs, again only two peaks were well defined, located at 6.2 Å and 7.5 Å (Figure 10b). Given their proximity, overlap made them difficult to distinguish in some models, and low numbers of PE lipids made the RDFs noisy in some replicates. No longer range structure was observed. Similarly, the PS lipids only present in the young adult models were not present in a sufficiently significant concentration for clear behavior (Figure 10c). Qualitatively, two peaks appear to be present, comparably to the PE RDFs.

The CER RDFs showed even more fluctuation due to small number of CER lipids in the simulations (Figure 10e). Only one very narrow peak was observed, and it was found at 4.6 Å. This suggests a stronger binding interaction that is less susceptible to fluctuations. A lack of long-range structure may simply be a consequence of low number of CER lipids.

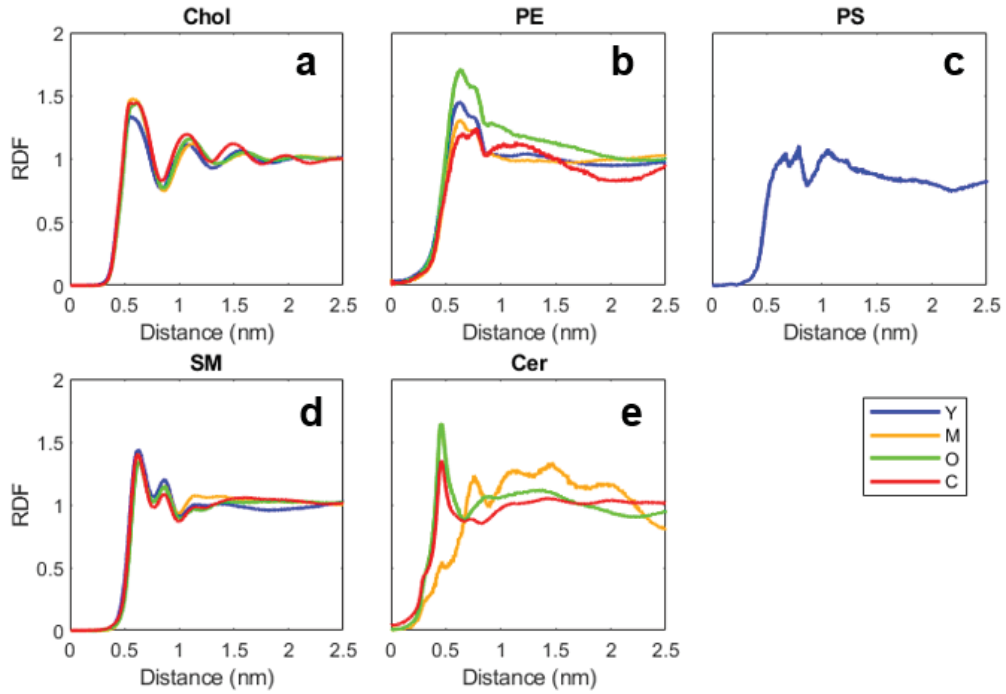

Figure 10. 2D-RDFs for self-interactions for each of the major headgroups present in the models, with (a) Chol, (b) PE, (c) PS, (d) SM, (e) CER.

Pairwise RDFs between Chol and the other lipid groups show long-range structure for all pairings (Figure 11). The distance between peaks is consistent across the four models, with shorter distances observed in the cataractous system. This is indicative of denser lateral packing of lipids

in the cataractous system. As with the self-interaction RDFs, the cataractous system also showed preservation of structure for the longest distances, with up to 4 observed peaks in the RDFs.

The SM and CER pairwise interactions with Chol show a smoothing of the first peak into an earlier appearing subpeak and the main peak (Figure 11c-d). This is likely due to the reference group on the SM and CER lipids being on the sphingosine backbone. Thus, rotational orientation of the lipid would lead to a loss of symmetry regarding interactions with its neighbors. This may be causing the broadening of the peaks. Choosing a group below the headgroup and glycerol backbone was necessary to compute the 2D RDFs due to Chol having an equilibrium position deeper in the membrane than the other lipids.

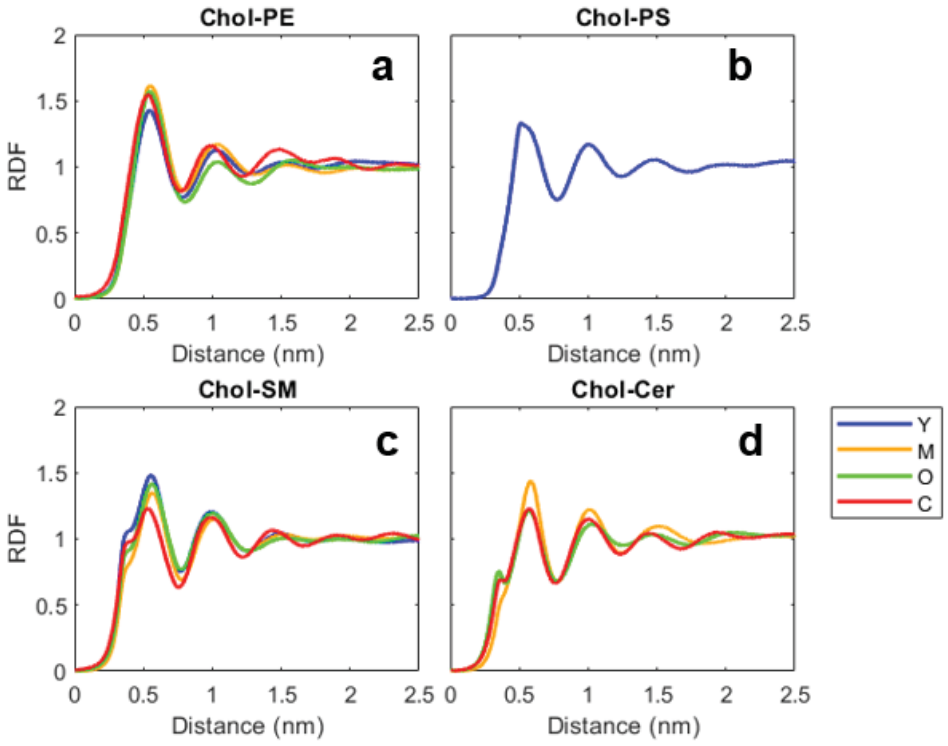

Figure 11. Pairwise RDFs between Chol and (a) PE, (b) PS, (c) SM, and (d) CER.

Clustering analyses showed that the composition of lipid clusters was roughly equal to the bulk composition of the membrane (Figure 12). CERs were underrepresented in clusters compared to their fraction of the membrane lipids. The neighbors of CER were determined by a smaller cutoff distance, although this distance was determined by the interaction length for CER from the RDFs. For clusters defined as 3 lipids or more, approximated 80% of lipids were in clusters at any

time frame, with the percentage in clusters decreasing in each age group (Table S1). More lipids were in clusters in the youngest age system compared to the middle- and older-aged systems, and the cataractous system showed the least clustering, although all were within 73-83% of lipids. This mirrors the increasing CER concentration, which may be indicative that the presence of ceramides may reduce the tendency to form clusters, as determined by headgroup interactions. It is possible this is due to the tendency of CER to position deeper in the membrane core due to its smaller headgroup. The size of clusters followed an approximately exponential pattern, with clusters of size 3 comprising around 20% of clusters and with only about one-third of clusters having 7 lipids or more (Figure S4). Larger clusters (more than 10 lipids) also had compositions reflective of the bulk membrane composition.

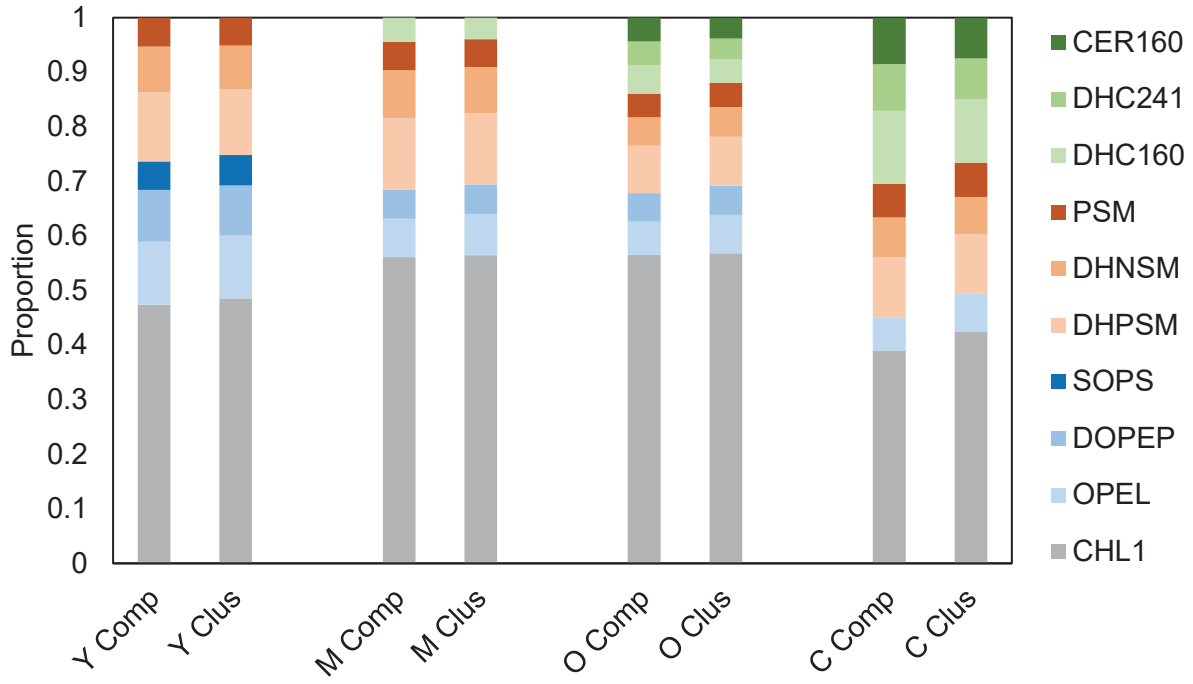

Figure 12. Distribution of lipids comparing compositions of the overall membrane to cluster compositions for each model.

3.9. Hydrogen Bonding (H bonding)

Hydrogen bonding was observed at similar levels in the middle-aged, older, and cataractous systems (Table 6). However, the young healthy model showed significantly higher levels of hydrogen bonding, particularly in the glycerophospholipids (OPEL, DOPEP, SOPS). This is likely due to the presence of the negatively charged PS lipid, only present in the youngest

system. Per lipid, SOPS engaged in 1.25±0.02 hydrogen bonds with other lipids. This high level of hydrogen bonding led to increases of around 50% in the number of hydrogen bonds formed in OPEL and DOPEP in the young system as compared to the other three systems. However, there was no notable change in the hydrogen bonding of the SMs and CERs between the systems. These lipids showed much more variation between replicates, leading to greater uncertainty in the number of hydrogen bonds. Typically, these lipids maintained between 0.4 and 0.7 hydrogen bonds per lipid across all replicates, with uncertainties up to around 0.05. Cholesterol engaged in little hydrogen bonding, with around 0.2 hydrogen bonds per lipid in all systems.

Table 6. Interlipid hydrogen bonds for each constituent lipid in each system.

	Y	**M**	**O**	**C**
Chol	0.237±0.005	0.220±0.002	0.188±0.005	0.27±0.02
DOPEP	1.02±0.02	0.696±0.004	0.67±0.03	-
OPEL	0.86±0.01	0.56±0.01	0.52±0.02	0.47±0.01
SOPS	1.25±0.02	-	-	-
PSM	0.7±0.04	0.62±0.02	0.56±0.05	0.71±0.07
DHPSM	0.73±0.07	0.65±0.02	0.59±0.03	0.69±0.04
DHNSM	0.63±0.05	0.62±0.06	0.74±0.02	0.65±0.04
CER160	-	-	0.38±0.07	0.6±0.1
DHC160	-	0.55±0.03	0.51±0.03	0.56±0.02
DHC241	-	-	0.46±0.06	0.59±0.03

4. Discussion

For studying ocular lens membranes, the low surface-area per lipid results suggest a very tightly packed membrane, characteristic of high-Chol concentration. All systems demonstrated high order, as characterized by narrow tilt angle distribution, high order parameter, and high compressibility modulus. Together, these observations indicate that all the models are within the liquid-ordered phase, where some lipids may be individually below their gel phase transition point, but the irregularity introduced by the Chol prevents crystallization. These quantitative observations underscore the importance of long timescale simulations to elucidate membrane behavior and overcome energy barriers in reaching the equilibrium state. Slight inconsistencies between the cataractous model replicates in this work may be a result of very slowly equilibrating systems due to high order and low lateral mobility. This model demonstrated the slowest equilibration in all metrics examined. While all performed analyses indicated uniformity over the period of analysis,

it is possible that systems were trapped in a local, but not global, energy minimum but since on the microsecond timescale these systems equilibrated these are likely stable states/configurations at least at this currently obtainable timescale. This is especially true of the older-aged and cataractous systems, which showed the highest degree of order and membrane rigidity.

Simulations of similar systems were previously conducted by Adams et al. to emulate human and bovine ocular lenses.[13] These systems contained five distinct lipids: Chol, DOPE, DPPC, NSM, and DHNSM. Of particular interest to this work were the systems of DOPE:NSM:Chol and DOPE:DHNSM:Chol, as DOPE is the diacyl counterpart to DOPEP and OPEL. General trends held between the systems examined in this study and the Chol:PE systems of Adams et al. [13]

A major result demonstrated by Adams et al. [13] was the significant effect of Chol in determining membrane properties. Control systems without Chol showed different phase behavior and markedly more fluidity than systems with Chol. Chol was associated with higher order parameter and greater D_{HH}. This work expands on that result by examining systems with varying concentrations of Chol. Experimental results suggest that the ocular lens becomes stiffer and more rigid with both increased age and the presence of cataracts (whether that is causal or correlative).[44] Naively, it might follow that an increase in the Chol concentration in the ocular lens drives the physiological changes. However, as noted in the introduction, studies suggest that the Chol concentration within the ocular lens membranes decreases with the presence of cataracts likely due to a decrease in solubility of Chol.[23] The models produced in this study ignore any precipitated Chol, and the cataractous system was studied with a decreased concentration of Chol. As noted previously, the cataractous system nonetheless demonstrated the highest order and rigidity, matching experimental results.

A possible explanation for how the cataractous system maintains a high degree of order despite a decrease in Chol is the sharp increase in CER and DHCER lipids. These lipids share features with Chol, such as only possessing an alcohol headgroup as opposed to a large phosphatidyl headgroup. CERs are significantly larger in the plane of the membrane with two tails but possess a similar ability to sit deeper within the hydrophobic core as compared to phospholipids. Thus, they have some functional similarities to Chol, and this may play a part in the observed increase in order in the cataractous system. Another possible cause is the decrease in

GLs. With almost all non-Chol lipids being SLs in the cataractous system, it is possible that wider networks of sphingosine interactions can form, contributing to membrane stability. However, significant increases were not observed in hydrogen bonds between healthy and cataractous systems, nor were significant changes in clustering phenomena.

5. Conclusion

Limited simulations had been performed studying the unique membrane compositions of ocular lens membranes. Lipid bilayers containing Chol, lysolipids, ether lipids, SM, DHSM, CER, and DHCER were analyzed, with compositions representing various age groups and the presence of cataracts. With increasing age group, an increase in membrane stiffness and order, both vertical and lateral, was observed. In addition, the cataractous models showed the highest degree of order and stiffness of all systems. These results match existing experimental evidence and suggest the ability of ceramides to increase order by efficient packing in a similar manner to Chol. The accuracy of the simulations to observed behavior suggest that these models may be an appropriate starting point for more complex simulations that consider the high density of membrane proteins within the ocular lens environment.

Given the high concentration of protein within the ocular lens membranes, future work can build on these findings by studying simulations of lens membranes that incorporate lens proteins. Little preferential clustering was observed within this study but favored protein-lipid interactions could drive the occurrence of a non-homogeneous distribution of lipids within the bilayer. These in turn could lead to deviations in membrane properties compared to those found here for pure lipid simulations. In addition, studies could be done to further understand the roles of unique lipids within the bilayer, including the lysolipids and plasmanyl lipids.

6. Acknowledgements

The computational resources used for this work were Deepthought2 maintained by the Division of Information Technology at the University of Maryland, as well as the resources of the Maryland Advanced Research Computing Center (MARCC). This work was in part supported by NSF (MCB-1951425 and CHE2003912). Model structures of the membranes discussed in this work can be obtained using the following link: https://terpconnect.umd.edu/~jbklauda/memb.html.

7. References

[1] V.L. Taylor, K.J. AlGhoul, C.W. Lane, V.A. Davis, J.R. Kuszak, M.J. Costello, Morphology of the normal human lens, Investigative Ophthalmology & Visual Science, 37 (1996) 1396-1410.

[2] D. Borchman, M.C. Yappert, M. Afzal, Lens lipids and maximum lifespan, Experimental Eye Research, 79 (2004) 761-768.

[3] D. Borchman, M.C. Yappert, Lipids and the ocular lens, Journal of Lipid Research, 51 (2010) 2473-2488.

[4] E. Cotlier, Y. Obara, B. Toftness, CHOLESTEROL AND PHOSPHOLIPIDS IN PROTEIN-FRACTIONS OF HUMAN LENS AND SENILE CATARACT, Biochimica Et Biophysica Acta, 530 (1978) 267-278.

[5] S.R. Ferguson, D. Borchman, M.C. Yappert, Confirmation of the identity of the major phospholipid in human lens membranes, Investigative Ophthalmology & Visual Science, 37 (1996) 1703-1706.

[6] M.C. Yappert, D. Borchman, Sphingolipids in human lens membranes: an update on their composition and possible biological implications, Chemistry And Physics Of Lipids, 129 (2004) 1-20.

[7] E. Plesnar, W.K. Subczynski, M. Pasenkiewicz-Gierula, Saturation with cholesterol increases vertical order and smoothes the surface of the phosphatidylcholine bilayer: A molecular simulation study, Biochimica Et Biophysica Acta-Biomembranes, 1818 (2012) 520-529.

[8] W.K. Subczynski, M. Raguz, J. Widomska, L. Mainali, A. Konovalov, Functions of Cholesterol and the Cholesterol Bilayer Domain Specific to the Fiber-Cell Plasma Membrane of the Eye Lens, Journal of Membrane Biology, 245 (2012) 51-68.

[9] R.F. Jacob, R.J. Cenedella, R.P. Mason, Direct evidence for immiscible cholesterol domains in human ocular lens fiber cell plasma membranes, Journal Of Biological Chemistry, 274 (1999) 31613-31618.

[10] M.C. Yappert, M. Rujoi, D. Borchman, I. Vorobyov, R. Estrada, Glycero-versus sphingo-phospholipids: correlations with human and non-human mammalian lens growth, Experimental Eye Research, 76 (2003) 725-734.

[11] R. Estrada, A. Puppato, D. Borchman, M.C. Yappert, Reevaluation of the phospholipid composition in membranes of adult human lenses by P-31 NMR and MALDI MS, Biochimica Et Biophysica Acta-Biomembranes, 1798 (2010) 303-311.

[12] J. Pól, V. Vidová, T. Hyötyläinen, M. Volný, P. Novák, M. Strohalm, R. Kostiainen, V. Havlíček, S.K. Wiedmer, J.M. Holopainen, Spatial Distribution of Glycerophospholipids in the Ocular Lens, PLOS ONE, 6 (2011) e19441.

[13] M. Adams, E. Wang, X.H. Zhuang, J.B. Klauda, Simulations of simple Bovine and Homo sapiens outer cortex ocular lens membrane models with a majority concentration of cholesterol, Biochimica Et Biophysica Acta-Biomembranes, 1860 (2018) 2134-2144.
[14] J.R. Hughes, J.M. Deeley, S.J. Blanksby, F. Leisch, S.R. Ellis, R.J.W. Truscott, T.W. Mitchell, Instability of the cellular lipidome with age, Age, 34 (2012) 935-947.
[15] I. López-Montero, F. Monroy, M. Vélez, P.F. Devaux, Ceramide: From lateral segregation to mechanical stress, Biochimica et Biophysica Acta (BBA) - Biomembranes, 1798 (2010) 1348-1356.
[16] L. Mainali, M. Raguz, W.J. O'Brien, W.K. Subczynski, Changes in the Properties and Organization of Human Lens Lipid Membranes Occurring with Age, Current Eye Research, 42 (2017) 721-731.
[17] M.J. Costello, S. Johnsen, S. Metlapally, K.O. Gilliland, L. Frame, D. Balasubramanian, Multilamellar spherical particles as potential sources of excessive light scattering in human age-related nuclear cataracts, Experimental eye research, 91 (2010) 881-889.
[18] M.J. Costello, T.N. Oliver, L.M. Cobo, Cellular architecture in age-related human nuclear cataracts, Investigative Ophthalmology & Visual Science, 33 (1992) 3209-3227.
[19] M.J. Costello, T.J. McIntosh, J.D. Robertson, Membrane specializations in mammalian lens fiber cells: Distribution of square arrays, Current Eye Research, 4 (1985) 1183-1201.
[20] W.-K. Lo, C.V. Harding, Square arrays and their role in ridge formation in human lens fibers, Journal of Ultrastructure Research, 86 (1984) 228-245.
[21] R.V.P. Tao, E. Cotlier, Ceramides of human normal and cataractous lens, Biochimica Et Biophysica Acta, 409 (1975) 329-341.
[22] L. Huang, V. Grami, Y. Marrero, D.X. Tang, M.C. Yappert, V. Rasi, D. Borchman, Human lens phospholipid changes with age and cataract, Investigative Ophthalmology & Visual Science, 46 (2005) 1682-1689.
[23] L. Mainali, M. Raguz, W.J. O'Brien, W.K. Subczynski, Properties of membranes derived from the total lipids extracted from clear and cataractous lenses of 61-70-year-old human donors, European Biophysics Journal with Biophysics Letters, 44 (2015) 91-102.
[24] J.M. Deeley, T.W. Mitchell, X.J. Wei, J. Korth, J.R. Nealon, S.J. Blanksby, R.J.W. Truscott, Human lens lipids differ markedly from those of commonly used experimental animals, Biochimica Et Biophysica Acta-Molecular and Cell Biology of Lipids, 1781 (2008) 288-298.
[25] L. Mainali, M. Raguz, W.J. O'Brien, W.K. Subczynski, Properties of membranes derived from the total lipids extracted from the human lens cortex and nucleus, Biochimica Et Biophysica Acta-Biomembranes, 1828 (2013) 1432-1440.
[26] S. Jo, T. Kim, V.G. Iyer, W. Im, CHARMM-GUI: A web-based graphical user interface for CHARMM, Journal of Computational Chemistry, 29 (2008) 1859-1865.

[27] S. Jo, T. Kim, W. Im, Automated builder and database of Protein/Membrane complexes for molecular dynamics simulations, PLoS One, 2 (2007) e880.
[28] E.L. Wu, X. Cheng, S. Jo, H. Rui, K.C. Song, E.M. Dávila-Contreras, Y. Qi, J. Lee, V. Monje-Galvan, R.M. Venable, J.B. Klauda, W. Im, CHARMM-GUI Membrane Builder toward realistic biological membrane simulations, Journal of Computational Chemistry, 35 (2014) 1997-2004.
[29] J.C. Phillips, R. Braun, W. Wang, J. Gumbart, E. Tajkhorshid, E. Villa, C. Chipot, R.D. Skeel, L. Kalé, K. Schulten, Scalable molecular dynamics with NAMD, Journal of Computational Chemistry, 26 (2005) 1781-1802.
[30] J.B. Klauda, R.M. Venable, J.A. Freites, J.W. O'Connor, D.J. Tobias, C. Mondragon-Ramirez, I. Vorobyov, A.D. MacKerell, R.W. Pastor, Update of the CHARMM All-Atom Additive Force Field for Lipids: Validation on Six Lipid Types, The Journal of Physical Chemistry B, 114 (2010) 7830-7843.
[31] Richard M. Venable, Alexander J. Sodt, B. Rogaski, H. Rui, E. Hatcher, Alexander D. MacKerell, Jr., Richard W. Pastor, Jeffery B. Klauda, CHARMM All-Atom Additive Force Field for Sphingomyelin: Elucidation of Hydrogen Bonding and of Positive Curvature, Biophysical Journal, 107 (2014) 134-145.
[32] A.N. Leonard, R.W. Pastor, J.B. Klauda, Parameterization of the CHARMM All-Atom Force Field for Ether Lipids and Model Linear Ethers, The Journal of Physical Chemistry B, 122 (2018) 6744-6754.
[33] W. Humphrey, A. Dalke, K. Schulten, VMD: Visual molecular dynamics, Journal of Molecular Graphics, 14 (1996) 33-38.
[34] W. Shinoda, S. Okazaki, A Voronoi analysis of lipid area fluctuation in a bilayer, The Journal of Chemical Physics, 109 (1998) 1517-1521.
[35] C. Das, M.G. Noro, P.D. Olmsted, Simulation Studies of Stratum Corneum Lipid Mixtures, Biophysical Journal, 97 (2009) 1941-1951.
[36] S. Louhichi, M. Gzara, H.B. Abdallah, A density based algorithm for discovering clusters with varied density, 2014 World Congress on Computer Applications and Information Systems (WCCAIS), 2014, pp. 1-6.
[37] R.M. Venable, F.L.H. Brown, R.W. Pastor, Mechanical properties of lipid bilayers from molecular dynamics simulation, Chemistry and Physics of Lipids, 192 (2015) 60-74.
[38] R. Gupta, B. Rai, Molecular Dynamics Simulation Study of Skin Lipids: Effects of the Molar Ratio of Individual Components over a Wide Temperature Range, The Journal of Physical Chemistry B, 119 (2015) 11643-11655.
[39] E. Wang, J.B. Klauda, Simulations of Pure Ceramide and Ternary Lipid Mixtures as Simple Interior Stratum Corneum Models, The Journal of Physical Chemistry B, 122 (2018) 2757-2768.

[40] B.A. Camley, M.G. Lerner, R.W. Pastor, F.L.H. Brown, Strong influence of periodic boundary conditions on lateral diffusion in lipid bilayer membranes, The Journal of Chemical Physics, 143 (2015) 243113.
[41] R.M. Venable, H.I. Ingólfsson, M.G. Lerner, B.S. Perrin, B.A. Camley, S.J. Marrink, F.L.H. Brown, R.W. Pastor, Lipid and Peptide Diffusion in Bilayers: The Saffman–Delbrück Model and Periodic Boundary Conditions, The Journal of Physical Chemistry B, 121 (2017) 3443-3457.
[42] M. Javanainen, H. Hammaren, L. Monticelli, J.-H. Jeon, M.S. Miettinen, H. Martinez-Seara, R. Metzler, I. Vattulainen, Anomalous and normal diffusion of proteins and lipids in crowded lipid membranes, Faraday Discussions, 161 (2013) 397-417.
[43] J.-H. Jeon, H.M.-S. Monne, M. Javanainen, R. Metzler, Anomalous Diffusion of Phospholipids and Cholesterols in a Lipid Bilayer and its Origins, Physical Review Letters, 109 (2012) 188103.
[44] R. Michael, A.J. Bron, The ageing lens and cataract: a model of normal and pathological ageing, Philosophical Transactions of the Royal Society B: Biological Sciences, 366 (2011) 1278-1292.